

## ROTATIONAL DYNAMICS AND STAR FORMATION IN THE NEARBY DWARF GALAXY NGC 5238

JOHN M. CANNON<sup>1</sup>, ANDREW T. McNICHOLS<sup>1,2</sup>, YARON G. TEICH<sup>1,3</sup>, CATHERINE BALL<sup>1</sup>, JOHN BANOVTZ<sup>1,4,5</sup>, ANNIKA BROCK<sup>1</sup>, BRIAN A. EISNER<sup>1</sup>, KATHLEEN FITZGIBBON<sup>1</sup>, MASAO MIAZZO<sup>1</sup>, ASRA NIZAMI<sup>1</sup>, BRIDGET REILLY<sup>1</sup>, ELIZABETH RUVOLO<sup>1</sup>, QUINTON SINGER<sup>1</sup>

*Accepted for publication in the Astronomical Journal*

### Abstract

We present new H I spectral line images of the nearby low-mass galaxy NGC 5238, acquired with the Karl G. Jansky Very Large Array (VLA<sup>a</sup>). Located at a distance of  $4.51 \pm 0.04$  Mpc, NGC 5238 is an actively star-forming galaxy with widespread H $\alpha$  and UV continuum emission. The source is included in many ongoing and recent nearby galaxy surveys, but until this work the spatially resolved qualities of its neutral interstellar medium have remained unstudied. Our H I images resolve the disk on physical scales of  $\sim 400$  pc, allowing us to undertake a detailed comparative study of the gaseous and stellar components. The H I disk is asymmetric in the outer regions, and the areas of high H I mass surface density display a crescent-shaped morphology that is slightly offset from the center of the stellar populations. The H I column density exceeds  $10^{21}$  cm<sup>-2</sup> in much of the disk. We quantify the degree of co-spatiality of dense H I gas and sites of ongoing star formation as traced by far-UV and H $\alpha$  emission. The neutral gas kinematics are complex; using a spatially-resolved position-velocity analysis, we infer a rotational velocity of  $31 \pm 5$  km s<sup>-1</sup>. We place NGC 5238 on the baryonic Tully-Fisher relation and contextualize the system amongst other low-mass galaxies.

*Subject headings:* galaxies: evolution — galaxies: dwarf — galaxies: irregular — galaxies: individual (NGC 5238)

### 1. INTRODUCTION

Nearby, star-forming dwarf galaxies are important laboratories for probing our understanding of the internal processes that govern low-mass halos. Systems within  $\sim 10$  Mpc can be resolved into individual stars, allowing detailed study of the interplay between recently-formed massive stars and the surrounding interstellar medium (ISM). With multi-wavelength supporting data and sufficient angular resolution of the H I 21-cm spectral line, we can also probe the dynamics of the sources and constrain the ratios of dark to baryonic matter.

The dwarf galaxies in the local volume have received significant attention in recent major surveys that span the electromagnetic spectrum. An incomplete list includes the GALEX ultraviolet (UV) imaging survey by Lee et al. (2011), the Hubble Space Telescope (HST) LEGUS UV survey by Calzetti et al. (2015), the HST optical survey ANGST by Dalcanton et al. (2009), and the SINGS, LVL, and KINGFISH surveys in the infrared (Kennicutt et al. 2003; Dale et al. 2009; Kennicutt et al. 2011). Taken as a whole, these surveys have revolutionized our understanding of low-mass galaxies; the panchromatic approach touches on multiple and diverse aspects of galaxy evolution, from massive star formation

to feedback to radiation balance in the ISM.

From the H I perspective, the nearby galaxy population has been studied in significant detail in multiple major interferometric surveys: WHISP (Westerbork H I Survey of Irregular and Spiral Galaxies; Swaters 2002), FIGGS (Faint Irregular Galaxies GMRT Survey; Begum et al. 2008), SHIELD (the Survey of H I in Extremely Low-mass Dwarfs; Cannon et al. 2011, Teich et al. 2016, McNichols et al. 2016), VLA-ANGST (Very Large Array Survey of ACS Nearby Galaxy Survey Treasury Galaxies; Ott et al. 2012), LITTLE-THINGS (Local Irregulars That Trace Luminosity Extremes in The H I Nearby Galaxy Survey; Hunter et al. 2012), and LVHIS (the Local Volume H I Survey; Kirby 2012). These surveys have provided a nearly complete observational census of the neutral hydrogen properties of the star-forming dwarfs in the local universe.

Since each of the aforementioned H I surveys has different selection criteria, there exist multiple local volume dwarf irregular galaxies that have not yet been studied in detail in the H I spectral line. Some of these systems also have extensive multi-wavelength observations from the UV to the infrared (e.g., from the aforementioned nearby galaxy surveys). One such system is NGC 5238 (also known as UGC 8565, VV 828, Mrk 1479, SBS 1332+518, IZw 64). Originally cataloged in Dreyer (1888), this nearby, actively star-forming galaxy has appeared in more than 100 peer-reviewed manuscripts. Remarkably, interferometric measurements of its neutral hydrogen have not been published until the present work. The proximity, low mass, and active star formation make it an interesting target for detailed observations of the neutral ISM.

NGC 5238 is resolved into stars in Sloan Digitized Sky Survey (SDSS) images, which reveal a blue stellar population and numerous prominent stellar clusters;

<sup>1</sup> Department of Physics & Astronomy, Macalester College, 1600 Grand Avenue, Saint Paul, MN 55105, USA

<sup>2</sup> NRAO Charlottesville, 520 Edgemont Road, Charlottesville, VA 22903-2475, USA

<sup>3</sup> Science Department, Somerville High School, 81 Highland Avenue, Somerville, MA 02143

<sup>4</sup> Department of Physics, MS-B1807, Hamline University, 1536 Hewitt Avenue, Saint Paul, MN 55104, USA

<sup>5</sup> Department of Physics and Astronomy, Purdue University, 525 Northwestern Avenue, West Lafayette, IN 47907, USA

<sup>a</sup> The National Radio Astronomy Observatory is a facility of the National Science Foundation operated under cooperative agreement by Associated Universities, Inc.

**Table 1**  
Basic Characteristics of NGC 5238

Parameter	Value
Right ascension (J2000)	13 <sup>h</sup> 34 <sup>m</sup> 42. <sup>s</sup> 5
Declination (J2000)	+51° 36′ 49″
Adopted distance (Mpc)	4.51 ± 0.04 <sup>a</sup>
M <sub>B</sub> (Mag.)	-14.61 <sup>b</sup>
M <sub>★</sub> (M <sub>⊙</sub> )	8.9 × 10 <sup>7c</sup>
Single-dish S <sub>HI</sub> (Jy km s <sup>-1</sup> )	5.77 ± 0.61 <sup>d</sup>
Interferometric S <sub>HI</sub> (Jy km s <sup>-1</sup> )	4.56 ± 0.46 <sup>e</sup>
Single-dish H I mass M <sub>HI</sub> (M <sub>⊙</sub> )	(2.8 ± 0.3) × 10 <sup>7d</sup>
Interferometric H I mass M <sub>HI</sub> (M <sub>⊙</sub> )	(2.2 ± 0.3) × 10 <sup>7e</sup>

<sup>a</sup> Tully et al. (2009)

<sup>b</sup> Modifying M<sub>B</sub> from Cook et al. (2014a) for the adopted distance.

<sup>c</sup> Modifying M<sub>★</sub> from Cook et al. (2014b) for the adopted distance.

<sup>d</sup> Thuan et al. (1999); note that those authors apply a +16% increase in the observed flux integral (4.98 ± 0.53 Jy km s<sup>-1</sup>) for beam effects.

<sup>e</sup> This work.

the central cluster shows very strong nebular emission lines. Broad-band HST images are used to derive a distance of 4.51 ± 0.04 Mpc in Tully et al. (2009); we adopt this distance throughout the present work, and show the resulting HST images below. NGC 5238 is included in the aforementioned LVL (Dale et al. 2009), GALEX UV (Lee et al. 2011), and LEGUS (Calzetti et al. 2015) surveys. Moustakas & Kennicutt (2006) use strong-line methods to derive a gas-phase oxygen abundance 12 + log(O/H) = 7.96 ± 0.20 (see also Marble et al. 2010), corresponding to Z ≈ 19% Z<sub>⊙</sub> using the Solar oxygen abundance of Asplund et al. (2009). Modifying the relevant values derived in those works for the updated distance, we collect global physical properties of NGC 5238 in Table 1.

The neutral hydrogen properties of NGC 5238 have only been studied with single-dish observations. Using the Nançay 300-m telescope, Thuan et al. (1999) find W<sub>50</sub> = 32 ± 4 km s<sup>-1</sup> and an observed H I line integral S<sub>HI</sub> = 4.98 ± 0.53 Jy km s<sup>-1</sup> (corrected to 5.77 ± 0.61 Jy km s<sup>-1</sup> for beam effects). At our adopted distance, NGC 5238 is a relatively low H I mass system, with M<sub>HI</sub> = (2.8 ± 0.3) × 10<sup>7</sup> M<sub>⊙</sub>; including a 35% correction for Helium and other metals, the total gas mass of NGC 5238 is (3.7 ± 0.3) × 10<sup>7</sup> M<sub>⊙</sub>. The source is comparable to the most massive galaxies in the SHIELD sample (Teich et al. 2016; McNichols et al. 2016); that program explicitly studies systems that inhabit the important but previously understudied mass range log(M<sub>HI</sub>) ≲ 10<sup>7.2</sup>, and we refer the reader to Teich et al. (2016) and McNichols et al. (2016) for details.

We organize this paper as follows. § 2 presents details about the new H I observations and the supporting datasets. § 3 presents the H I properties of NGC 5238, including a quantitative comparison of the degree of co-spatiality between star formation rate tracers (Hα and far-UV emission) and H I mass surface densities. § 4 examines the complex neutral gas kinematics of NGC 5238. In § 5 we contextualize NGC 5238 against the SHIELD galaxies, and in § 6 we draw our conclusions.

## 2. OBSERVATIONS AND DATA HANDLING

### 2.1. HI Observations

HI spectral-line observations of NGC 5238 were acquired with the Karl G. Jansky Very Large Array (VLA) in the C configuration on February 1, 2016 for program TDEM0021. This program was executed under the auspices of the “Observing for University Classes” program, a service provided by the NRAO as an opportunity for courses teaching radio astronomy theory to acquire new observations to be analyzed by students. All of the results in this manuscript stem from the efforts of undergraduate students at Macalester College.

The WIDAR correlator divides a 4.0 MHz bandwidth into 1,024 channels, delivering a native spectral resolution of 0.86 km s<sup>-1</sup> ch<sup>-1</sup>. The primary and phase calibrators were J1331+305 (3C 286) and J1400+621, respectively. The total on-source integration time was approximately 1.6 hours. The VLA data were calibrated using standard prescriptions in the AIPS<sup>6</sup> and CASA<sup>7</sup> environments. Imaging of the J1400+6210 phase calibrator field yielded a flux density S<sub>ν</sub> = 4.24 ± 0.01 Jy. Continuum subtraction of the NGC 5238 field was performed in the *uv* plane using a first-order fit to line-free channels bracketing the galaxy in the central 50% of the bandpass.

Imaging of the calibrated *uv* visibilities followed standard prescriptions similar to those described in Cannon et al. (2015) and in Teich et al. (2016). In brief, the input continuum-subtracted database was spectrally smoothed by a factor of two, to produce a velocity resolution of 7.812 kHz ch<sup>-1</sup> (1.56 km s<sup>-1</sup> ch<sup>-1</sup>). The cube was then inverted and cleaned using the IMAGR task in AIPS; the ROBUST factor is 0.5. Cleaning was performed to 2.5 times the rms noise per channel in line-free channels. Residual flux rescaling was enforced during the imaging process (Jorsater & van Moorsel 1995). The resulting synthesized beam size of 17.69″ × 15.40″ was smoothed to a circular 18″ beam. The rms noise in the final 18″ cube is 1.4 mJy Bm<sup>-1</sup>.

Two-dimensional moment maps were produced from the three-dimensional datacube as follows. The original 17.69″ × 15.40″ cube was first spatially smoothed by a Gaussian kernel to a beam size of 30″. Using the rms noise in this cube, a threshold mask was applied at the 2.5σ level. The resulting cube was then examined by hand to isolate real emission, which is required to be both spectrally and spatially coincident across three neighboring channels. The resulting blanked cube was used as a transfer mask against the 18″ beam cube. The result was collapsed to create traditional moment maps representing H I mass surface density, intensity weighted velocity field, and velocity dispersion.

### 2.2. Multiwavelength Archival Observations

We compare our new H I images with archival ground and space-based imaging in order to study the stellar populations in NGC 5238. Calibrated images in the SDSS *g*, *r*, and *i* filters were obtained from the SDSS public website (York et al. 2000). Archival HST images from programs 10905 (Advanced Camera for Surveys, F606W and F814W filters) and 13364 (Wide Field Planetary Camera 3, F275W, F336W, F438W filters, from the

<sup>6</sup> Developed and maintained by NRAO

<sup>7</sup> <https://casa.nrao.edu>

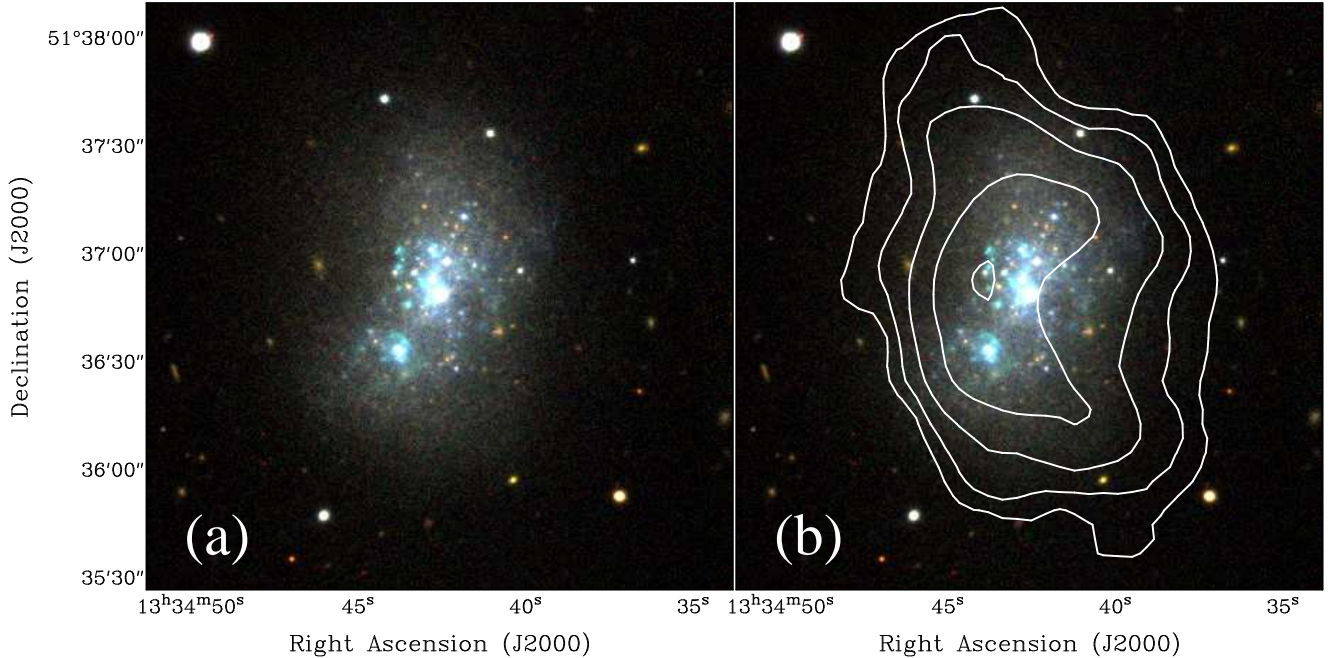


**Figure 1.** SDSS 3-color image of NGC 5238; SDSS g,r,i filters are blue, green, and red, respectively. NGC 5238 is marginally resolved into individual stars in ground-based images.

LEGUS survey; Calzetti et al. 2015) allow us to study the stellar populations at the highest angular resolutions, from the near-UV to the near-IR. We use these images to construct color mosaic images of NGC 5238. The LEGUS data (Calzetti et al. 2015) highlight the young stellar populations, while the optical data highlight the older stellar populations (and some nebular emission).

Continuum-subtracted  $H\alpha$  images are acquired from the LVL survey data products (Kennicutt et al. 2008). The Bok 2.3 m telescope was used to image NGC 5238 in the standard  $H\alpha$  and R-band filters. A bright foreground star is located in close angular proximity to the central stellar cluster in NGC 5238. This object leaves artifacts from continuum subtraction in the field; we discuss this source in more detail below. The total  $H\alpha$  luminosity of NGC 5238 derived by Kennicutt et al. (2008) is corrected for foreground extinction. Scaling this value from 5.2 Mpc to the new distance of 4.51 Mpc, we find  $\log(L_{H\alpha}) = 39.09$ , corresponding to  $\log(\text{SFR}_{H\alpha}) = -2.01 M_{\odot} \text{ yr}^{-1}$  using the star formation rate calibration from Kennicutt (1998).

GALEX far-UV (FUV) and near-UV (NUV) imaging of NGC 5238 is presented in Lee et al. (2011). The source is detected at high significance in both filters, indicating recent star formation over the last few hundred Myr. Lee et al. (2011) calculates the total extinction-corrected FUV magnitude from NGC 5238,  $m_{\text{FUV}} = 15.19 \pm 0.05$ . Using the star formation rate calibration derived in McQuinn et al. (2015), this corresponds to  $\log(\text{SFR}_{\text{FUV}}) = -1.81 M_{\odot} \text{ yr}^{-1}$  at our adopted distance; note that this star formation rate is slightly higher than using the star formation rate metric from Hao et al. (2011), which gives  $\log(\text{SFR}_{\text{FUV}}) = -2.00 M_{\odot} \text{ yr}^{-1}$ .

### 3. NEUTRAL GAS AND STAR FORMATION IN NGC 5238

#### 3.1. The HI Properties of NGC 5238

In Figure 1 we present a first-order comparison of the gaseous and stellar components of NGC 5238. The H I mass surface density distribution (discussed in more detail below) is overlaid as contours on a 3-color SDSS image. The outer H I disk is asymmetric; the morphological major axis is elongated from northeast to southwest. The high column density H I gas shows a crescent-shaped morphology. The H I surface density maximum is not coincident with the central optical peak, but rather is offset to the northeast by  $\sim 300$  pc; such offsets are not unusual in dwarf galaxies (see, e.g., van Zee et al. 1997; Hunter et al. 1998). The H I disk is slightly larger than the high surface brightness optical body; the SDSS Petrosian-r radius ( $45''$ ) can be compared to the size of the H I disk ( $\sim 90''$  radius at the level of  $10^{20} \text{ cm}^{-2}$ ).

The H I spectral line is detected at high significance across roughly 25 channels ( $\sim 40 \text{ km s}^{-1}$ ) of the final  $18''$  datacube. Figure 2 shows individual channel maps of the H I emission across which gas is detected. Summing the emission across these channels produces the global H I profile shown in Figure 3. As expected based on the galaxy's low mass, the profile is Gaussian-like with no obvious double-horn structure. Using the intensity-weighted average of the global H I profile, the systemic velocity is  $V_{\text{HI}} = 232 \pm 1 \text{ km s}^{-1}$ ; this is in good agreement with  $V_{\text{HI}} = 235 \pm 2 \text{ km s}^{-1}$  derived in Thuan et al. (1999).

Integrating the detected flux from NGC 5238 produces the moment maps shown in Figure 4. As noted above, the high mass surface density H I gas ( $N_{\text{HI}} \gtrsim 10^{21} \text{ cm}^{-2}$ , shown by the white contour in Figure 4) displays a crescent-shaped morphology. The peak H I column density is  $1.67 \times 10^{21} \text{ cm}^{-2}$ , which corresponds to an H I mass surface density of  $13.4 M_{\odot} \text{ pc}^{-2}$ . We discuss the H I mass surface density and its relation to the ongoing and recent star formation in more detail in § 3.2.

The H I moment one map, representing intensity-

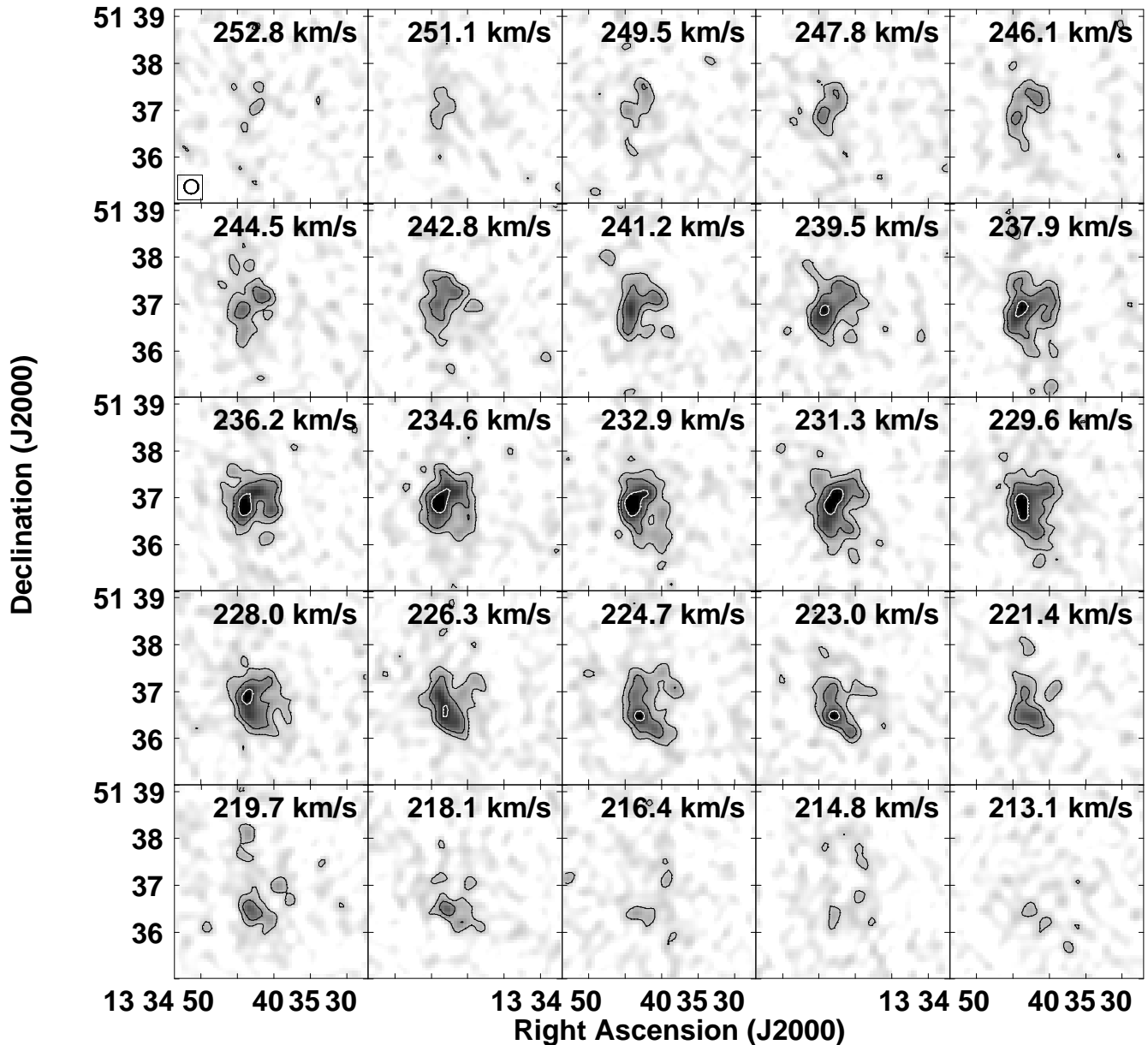


**Figure 2.** Channel maps of NGC 5238. Contours are overlaid at  $3\sigma$ ,  $6\sigma$ , and  $12\sigma$ , where  $\sigma$  is the rms noise in line-free channels of the HI cube ( $\sigma = 1.4 \times 10^{-3}$  Jy Bm $^{-1}$ ). The circular  $18''$  beam size is shown in the bottom left of the first panel.

weighted H I velocity, is shown as panel (b) of Figure 4. As discussed in detail in McNichols et al. (2016), the collapse of the three-dimensional cube to two dimensions results in a more narrow velocity width of the source; by comparing Figures 2 and 4, it is clear that H I gas is detected over  $\sim 40$  km s $^{-1}$  in the data cube but that the resulting velocity field only captures  $\sim 20$  km s $^{-1}$ . Examining the velocity field, the H I kinematics are complex. There is a velocity gradient extending from southwest to northeast along a position angle of roughly  $20^\circ$  (east of north). However, significant velocity asymmetries are present throughout the disk; there is an S-shaped velocity profile that may be suggestive of a warp in the disk. We discuss the neutral gas kinematics in detail in § 4.

The H I moment two map shows velocity disper-

sions ranging from 7-12 km s $^{-1}$ , in good agreement with characteristic values determined from H I observations of many types of galaxies (e.g., Tamburro et al. 2009; Ianjamasimanana et al. 2015; Mogotsi et al. 2016) and in particular for values determined for local volume dwarf galaxies (e.g., Hunter et al. 2012; Ott et al. 2012). We note that the H I column density maximum is coincident with gas with  $\sigma \simeq 8$  km s $^{-1}$ . Similarly, in the inner regions of the disk with active star formation, the H I velocity dispersion remains below 10 km s $^{-1}$ .

In terms of H I content, NGC 5238 can be directly compared with the sample of 12 SHIELD galaxies presented in Teich et al. (2016) and McNichols et al. (2016). NGC 5238 has an H I mass comparable to the most massive SHIELD galaxies; only AGC 749237 is more H I-

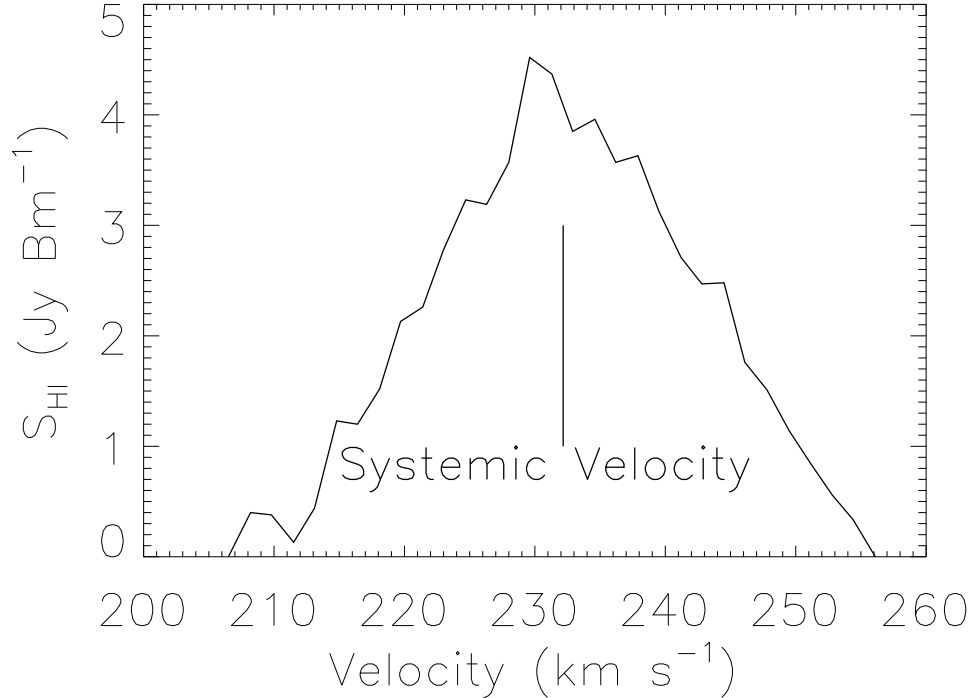


**Figure 3.** Global H I profile of NGC 5238, created by summing the flux in each channel of the  $18''$  resolution blanked datacube. The H I systemic velocity, derived from an intensity weighted mean of the spectrum, is  $V_{\text{HI}} 232 \pm 1 \text{ km s}^{-1}$ .

massive. The peak H I column density in NGC 5238 is equal to the peaks found in AGC 110482 and in AGC 749237. In the following sections we further contextualize NGC 5238 against the SHIELD sources.

### 3.2. Comparing Stellar Population and Neutral Gas Properties

NGC 5238 is an actively star-forming dwarf galaxy (see § 2.2). Using  $\text{H}\alpha$  emission as a recent star formation rate indicator (within the last 10 Myr),  $\log(\text{SFR}_{\text{H}\alpha}) = -2.01 \text{ M}_{\odot} \text{ yr}^{-1}$ . Averaged over a longer timescale of  $\sim 100$  Myr, the GALEX far-UV emission indicates a star formation rate that is  $\sim 60\%$  higher:  $\log(\text{SFR}_{\text{FUV}}) = -1.81 \text{ M}_{\odot} \text{ yr}^{-1}$ . Each of these star formation rates are higher than those of any of the SHIELD galaxies.

To compare the neutral gas properties with the locations of recent star formation in NGC 5238, in Figure 5 we show multi-wavelength imaging compared to the H I mass surface density. The fields of view are the same in all panels. The H I column density contours highlight regions above  $10^{21} \text{ cm}^{-2}$ . This mass surface density level has been empirically identified as the requisite level for massive star formation as traced by  $\text{H}\alpha$  emission (Skillman 1987); note that more recent studies have shown that such a surface density is not universal (e.g., Bigiel et al. 2008, Elmegreen & Hunter 2015, Teich et al. 2016, and the various references therein). The aforementioned crescent-shape morphology is very prominent in the highest column density gas.

The HST images shown in panels (a) and (b) of Figure 5 dramatically resolve the stellar populations in NGC 5238. The LEGUS image (Calzetti et al. 2015)

shown in panel (a) clearly highlights the youngest stellar clusters. The most prominent of these structures is located in the southern region of the galaxy (coincident with the southern-most extension of the  $1.4 \times 10^{21} \text{ cm}^{-2}$  column density contour); nebular emission (arising from the  $\text{H}\alpha$  spectral line, which falls in the F606W filter) surrounds this cluster in the optical image shown in panel (b). Smaller young clusters, identified by a comparison of panels (a) and (b), are located in the regions of highest H I column density ( $N_{\text{HI}} \gtrsim 16 \times 10^{20} \text{ cm}^{-2}$ , in the northeast region of the optical body) as well as in the optical center. A close inspection of panel (b) reveals that nebular emission is associated with all of these clusters, and is brightest near the central, bright cluster.

As expected, the nebular emission visible in the HST image matches the morphology of the continuum-subtracted  $\text{H}\alpha$  image shown in panel (d). The ground-based  $\text{H}\alpha$  image has better surface brightness sensitivity due to the comparatively narrow filter width; this image clearly reveals widespread  $\text{H}\alpha$  emission throughout the galaxy. The most  $\text{H}\alpha$ -luminous region is the central stellar cluster, followed closely by the strong  $\text{H}\alpha$  emission from the young stellar cluster in the southern disk. In addition to these two major maxima, there is  $\text{H}\alpha$  emission throughout the disk (including regions associated with obvious UV clusters in the LEGUS HST image) and also multiple dramatic loops and arcs that extend significantly beyond the locations of the most luminous clusters (for example, the nearly circular structure extending to the western edge of the disk).

NGC 5238 harbors widespread UV emission in both

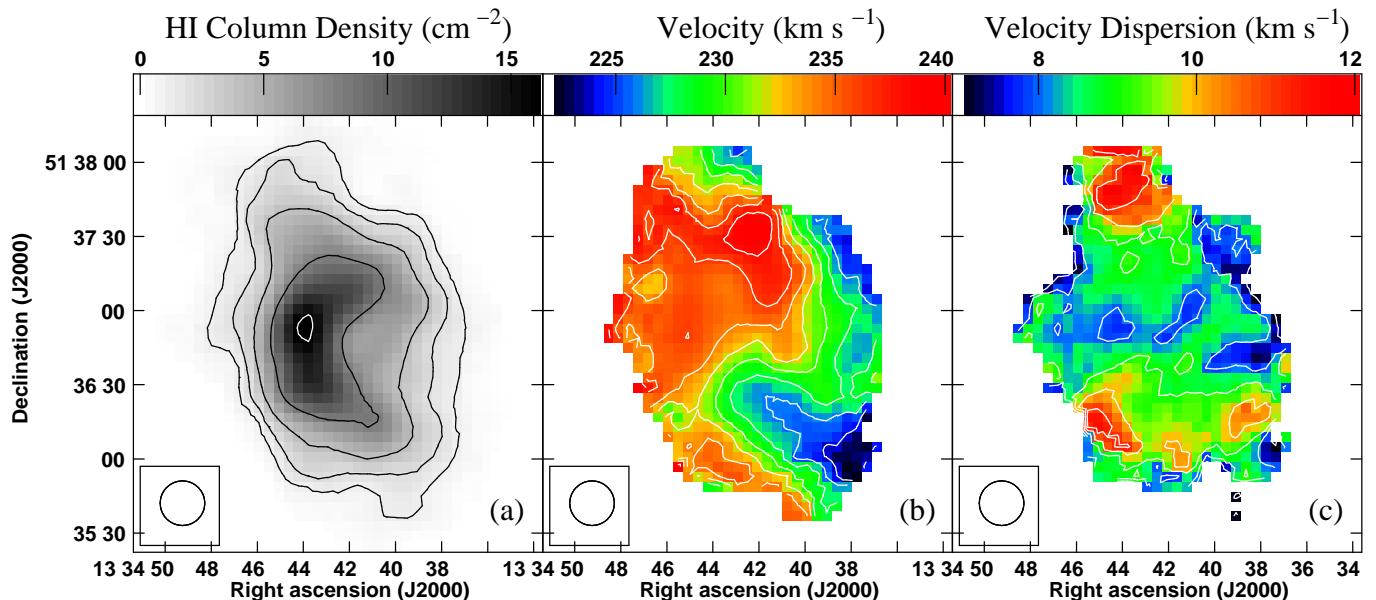


**Figure 4.** H I moment maps of NGC 5238. Panel (a) shows the H I mass surface density in units of atoms  $\text{cm}^{-2}$ ; contours are at levels of  $(1,2,4,8,16) \times 10^{20} \text{ cm}^{-2}$ . Panel (b) shows the intensity-weighted velocity field; contours span the range 224 – 238  $\text{km s}^{-1}$ , spaced by 2  $\text{km s}^{-1}$  per contour. Panel (c) shows the velocity dispersion of the H I gas; contours span the range 7 – 11  $\text{km s}^{-1}$ , spaced by 1  $\text{km s}^{-1}$  per contour (note that this separation is formally smaller than our spectral resolution). The  $18''$  circular beam size is shown in the bottom left of each panel.

the GALEX FUV and the NUV bands. As panel (c) of Figure 5 shows, the UV emission peaks in two prominent clusters that match with the highest surface brightness  $\text{H}\alpha$  regions and with the prominent UV clusters in the LEGUS images. There is also widespread UV emission throughout the rest of the stellar disk, including emission from young, blue stars that trace the loop structure that is seen in  $\text{H}\alpha$  on the western side of the disk.

When interpreting Figure 5, it is important to note that there is a bright foreground star in close angular proximity to the central young cluster. This object appears somewhat pink in the LEGUS image in Figure 5, and is evident as an imperfectly-subtracted image artifact in the  $\text{H}\alpha$  image. The SDSS spectroscopic aperture contains this source; emission lines are nonetheless very prominent in the resulting spectrum (not shown here), which is centered on the  $\text{H}\alpha$  surface brightness maximum that is slightly offset to the east.

### 3.3. Quantifying Star Formation and Neutral Gas Properties

As discussed in the preceding sections, the widespread recent star formation in NGC 5238 is occurring in a variety of physical conditions. The regions of highest H I mass surface density are  $\text{H}\alpha$  and UV-luminous; however, the H I column density maximum is not coincident with the UV or with the  $\text{H}\alpha$  maxima. Similarly, there is some recent star formation occurring in regions of lower H I column densities (i.e., outside of the lowest contour shown in Figure 5,  $N_{\text{HI}} = 10^{21} \text{ cm}^{-2}$ ); such emission is especially prominent in the western portion of the disk.

We now seek to quantify the degree of co-spatiality (or lack thereof) between H I mass surface density and the tracers of recent star formation (FUV and  $\text{H}\alpha$  emission). Numerous recent works have investigated empirical thresholds for star formation in the neutral and

molecular ISM (e.g., Skillman 1987; Bigiel et al. 2008; Roychowdhury et al. 2014; Elmegreen & Hunter 2015; Teich et al. 2016); no single prescription has yet been identified that holds in all environments. For uniformity, thus we follow the procedures outlined in Teich et al. (2016) by deriving the index of the “Schmidt-Kennicutt” relation (Schmidt 1959), which relates a star formation rate surface density to a gas surface density:

$$\Sigma_{\text{SFR}} \propto (\Sigma_{\text{gas}})^N \quad (1)$$

where the star formation rate surface density ( $\Sigma_{\text{SFR}}$ ) is in units of  $M_{\odot} \text{ yr}^{-1} \text{ kpc}^{-2}$ , the gas surface density ( $\Sigma_{\text{gas}}$ ) in units of  $M_{\odot} \text{ pc}^{-2}$ , and  $N$  is a positive number. Specifically, we compare the star formation rate surface densities (hereafter,  $\Sigma_{\text{FUV SFR}}$  for FUV and  $\Sigma_{\text{H}\alpha \text{ SFR}}$  for  $\text{H}\alpha$ ) against the H I mass surface densities (hereafter,  $\Sigma_{\text{HI}}$ ) on both a radially-averaged and on a pixel-by-pixel basis. Note that because of the comparatively low star formation rates (and correspondingly low  $\text{H}\alpha$  fluxes) of the SHIELD galaxies, Teich et al. (2016) did not significantly interpret  $\text{H}\alpha$ -based radial profiles and did not show the  $\text{H}\alpha$ -based pixel-by-pixel correlation functions. In contrast, in NGC 5238 the higher star formation rate and more widespread  $\text{H}\alpha$  emission allows us to examine trends using both instantaneous and longer-timescale metrics.

In order to extract these diagnostics, the FUV,  $\text{H}\alpha$ , and H I moment 0 images are placed on the same coordinate grid. For the radially averaged profiles, the HST F606W image is used to fit stellar surface brightness as a function of radius with the CLEAN GALAXY code (Hagen et al. 2014). This program identifies a central aperture location (in this case, spatially coincident with the FUV and  $\text{H}\alpha$  surface brightness maxima), the major and minor axis lengths of concentric ellipses in the fit, and the position angle of those ellipses. For NGC 5238, the el-

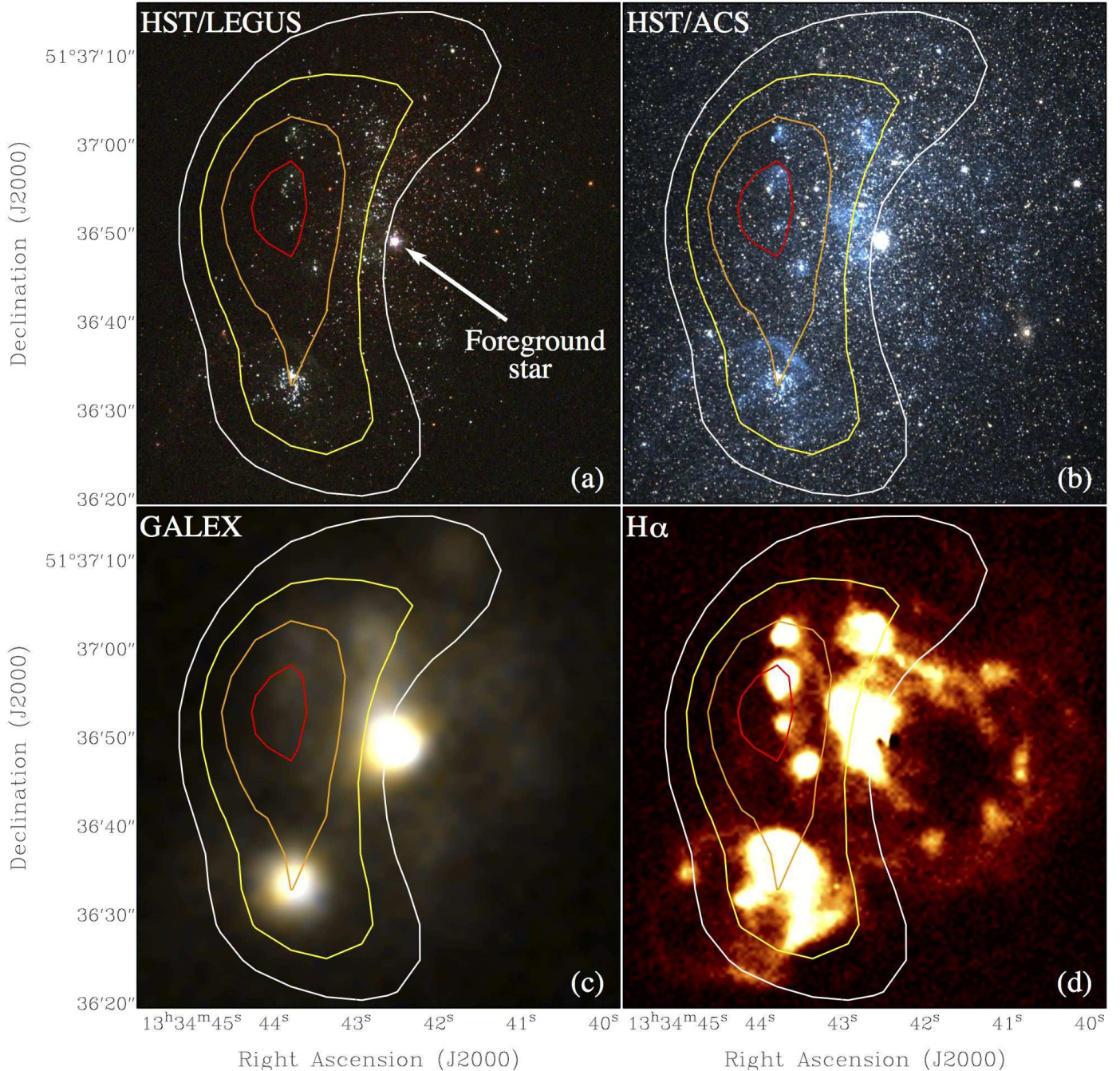


**Figure 5.** Comparison of high mass surface density H I gas with multi-wavelength imaging of NGC 5238. H I column density contours are shown at levels of  $(10,12,14,16) \times 10^{20} \text{ cm}^{-2}$  by white, yellow, orange, and red contours, respectively. Panel (a) shows the 3-color HST image from the LEGUS survey (F275W in blue, F336W in green, F438W in red). Panel (b) shows the 3-color HST image using archival ACS imaging (F606W in blue, F814W in red, and the linear combination of the two filters as green). Panel (c) shows the UV emission detected by GALEX (far-UV channel in blue, near-UV channel in red, and the linear combination of the two filters as green). Panel (d) shows the continuum-subtracted H $\alpha$  image from the LVL survey data products (Kennicutt et al. 2008). The arrow in panel (a) denotes the location of the Milky Way foreground star.

lenses are centered at  $(\alpha, \delta) = 13^{\text{h}}34^{\text{m}}42.7^{\text{s}}, +51^{\circ}36'50.5''$  (J2000), with an axial ratio of 1.54 and a position angle (measured east of north) of  $160^{\circ}$ . Following the discussion in Haurberg (2013), this corresponds to an optical inclination of  $50^{\circ}$ , which is used to deproject values per unit area. Surface brightnesses in H I, FUV, and H $\alpha$  are then extracted using either these concentric apertures (for the radially-averaged method) or in individual, matched pixels (for the pixel-by-pixel method).

The results of the radially-averaged analysis are shown in Figure 6. As expected based on the qualitatively similar morphologies and the similar global star formation rates in the FUV and in H $\alpha$ , these radial profiles are effectively the same using either tracer. The H I profile is less centrally peaked and follows a shallower slope as a function of increasing galactocentric radius. In general, this plot demonstrates that low H I mass surface densities are typically associated with lower star forma-

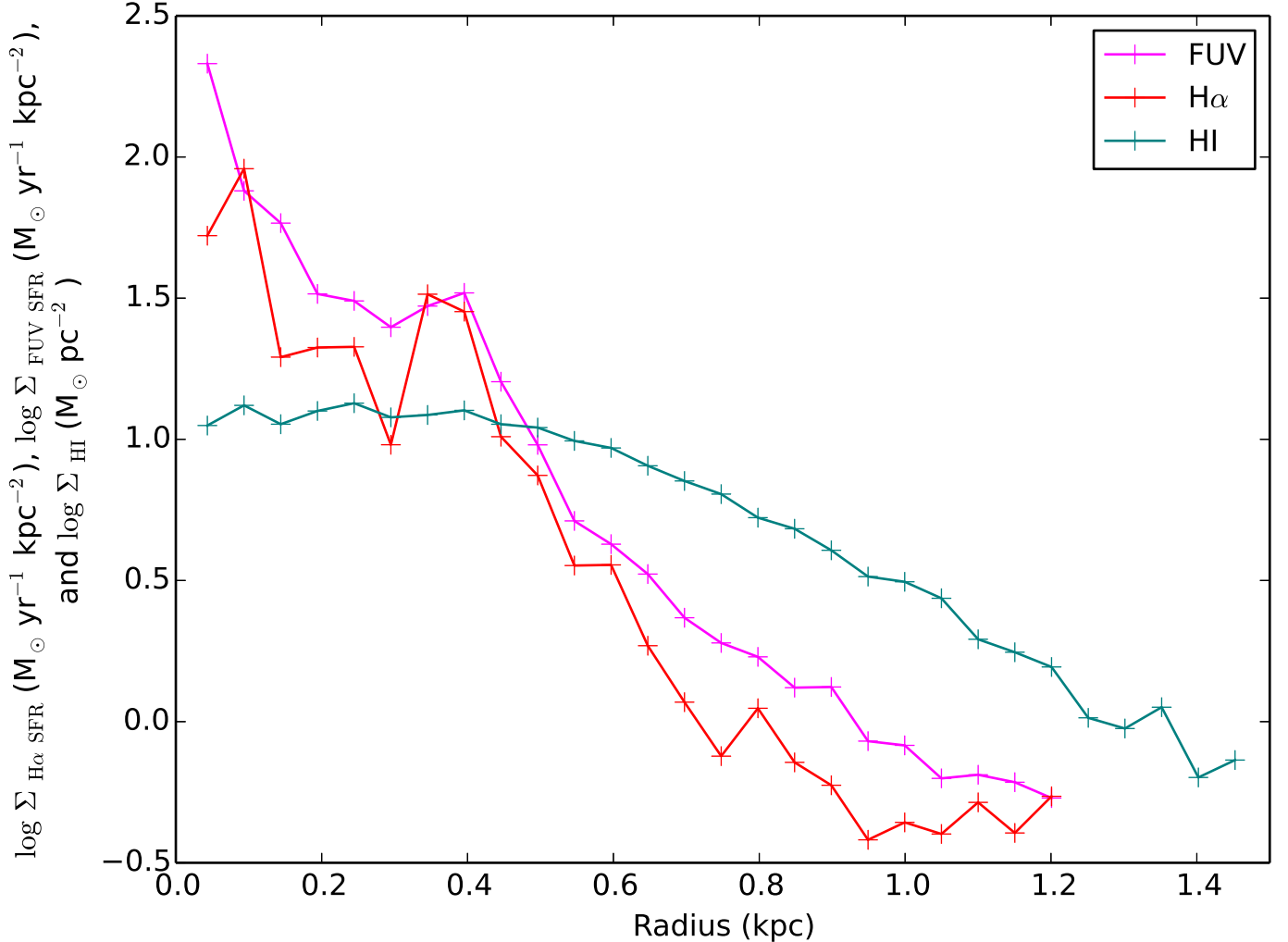


**Figure 6.**  $\Sigma_{\text{H}\alpha}$  SFR,  $\Sigma_{\text{FUV}}$  SFR, and  $\Sigma_{\text{H I}}$  and vs. radius for NGC 5238. These plots allow us to examine the radially averaged trends of star formation rate surface density and H I mass surface density.

tion rate surface densities. However, it also makes clear that the regions of highest star formation rate surface density are associated with gas at a range of H I mass surface densities; in the inner  $\sim 500$  pc of the disk, the star formation rate surface densities vary by an order of magnitude in annuli where the H I mass surface density is effectively constant.

The radial integration used to create Figure 6 smears out localized variations in star formation rate surface density and H I mass surface density. To overcome this limitation, we quantify the localized relations between H I, H $\alpha$ , and FUV emission using the pixel-by-pixel correlation analysis shown in Figure 7. The top and bottom panels show the FUV and the H $\alpha$ -based star formation rate surface densities as functions of the H I mass surface density on a pixel-by-pixel basis. These plots quantify the local star formation law via the Schmidt-Kennicutt formalism; the power-law index using each tracer is shown in each panel. The FUV slope ( $N = 1.46 \pm 0.02$ ) is slightly steeper than the H $\alpha$  slope ( $N = 1.17 \pm 0.01$ ), suggesting a slightly stronger correlation between FUV-bright regions and the highest H I mass surface densities. However, these plots also highlight the

ongoing and recent star formation in NGC 5238 that is occurring outside the regions of densest H I gas. The “canonical”  $10^{21} \text{ cm}^{-2}$  column density threshold (corresponding to  $7.9 \text{ M}_\odot \text{ pc}^{-2}$ ) is denoted by a vertical dotted line; while most of the highest star formation rate surface densities occur above this H I mass surface density level, this is not a requirement. A significant amount of star formation is associated with H I gas that is “sub-critical”.

#### 4. THE DYNAMICS OF NGC 5238

Low-mass galaxies such as NGC 5238 offer a unique opportunity to populate the low-mass, low-velocity end of the baryonic Tully-Fisher relation (Tully & Fisher 1977; see also McGaugh 2012, McNichols et al. 2016, and the various references therein). These low-mass systems are critical for our understanding of this fundamental scaling relation that holds over many orders of magnitude for more massive galaxies. Importantly, gas-rich systems in this mass regime allow us to determine the rotational dynamics by spectral lines; gas-poor systems must rely on dispersion measurements from stars.

As discussed at length in McNichols et al. (2016), ex-



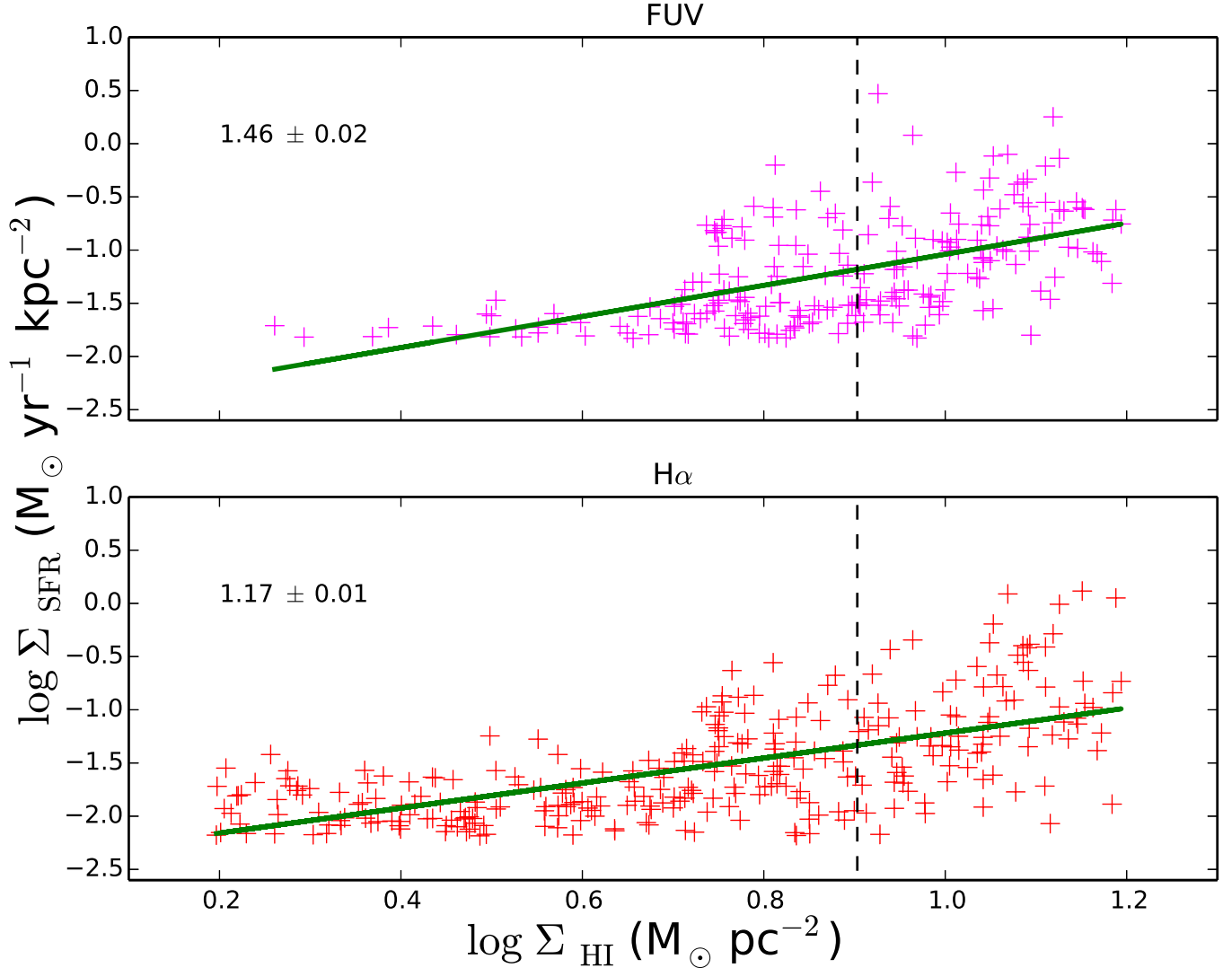


**Figure 7.**  $\Sigma_{\text{H}\alpha \text{ SFR}}$  vs.  $\Sigma_{\text{H I}}$  (top) and  $\Sigma_{\text{FUV SFR}}$  vs.  $\Sigma_{\text{H I}}$  (bottom) for NGC 5238. All FUV and H $\alpha$  pixel values higher than 5% of the maximum are plotted; for H I all pixels higher than 10% of the maximum are plotted. A positive slope indicates high FUV and H I emission in the same pixels. The dashed vertical line represents the column density threshold of  $1 \times 10^{21}$  atoms  $\text{cm}^{-2}$ . The power-law best fit slopes are shown; these correspond to the Kennicutt-Schmidt indices discussed in the text.

tracting unambiguous information about the dynamics of low-mass galaxies is notoriously difficult. That work identifies an empirical threshold of  $15 \text{ km s}^{-1}$ , below which pressure support and coherent rotation can no longer be differentiated. Modeling in three spatial dimensions is preferable to using collapsed two-dimensional representations of the data (compare, for example, the channel maps shown in Figure 2 to the intensity weighted velocity field shown in Figure 4). However, in most cases, degeneracies between inclination and rotation velocity make three-dimensional work insufficiently constrained for unambiguous solutions.

Following the methodologies in McNichols et al. (2016), which include both two- and three-dimensional modeling approaches, we are not able to produce an unambiguous model of the rotational dynamics of NGC 5238 with the present data. Attempts were made to model the system as an asymmetrically distributed gas disk exhibiting coherent rotation with a strong warp. These challenges may be expected based on the narrow

H I line width and the complex kinematics apparent in the two-dimensional velocity field (Figure 4).

For uniformity we thus perform a spatially resolved position-velocity (hereafter, P-V) analysis in NGC 5238. We first identify the kinematic major axis by inspection as that axis along which the projected velocity extent is largest. This major axis P-V slice (of width equal to the H I beam size,  $18''$ ) is centered at  $\alpha, \delta = (13^{\text{h}}34^{\text{m}}42.5^{\text{s}}, +51^{\circ}36'49.0'')$ , J2000) and follows a position angle of  $20^{\circ}$  east of north; this axis is evident in the two-dimensional velocity field shown in Figure 4. Note that this kinematic major axis not aligned with the optical major axis identified in § 3.3 ( $160^{\circ}$  east of north, or  $20^{\circ}$  west of north); the two axes differ by  $\sim 40^{\circ}$ . Such misalignments of the optical and H I major axes are common in the SHIELD galaxies.

Minor axis P-V slices (position angle =  $290^{\circ}$  east of north) are extracted at positions along the kinematic major axis, separated by the H I beam width ( $18''$ ).

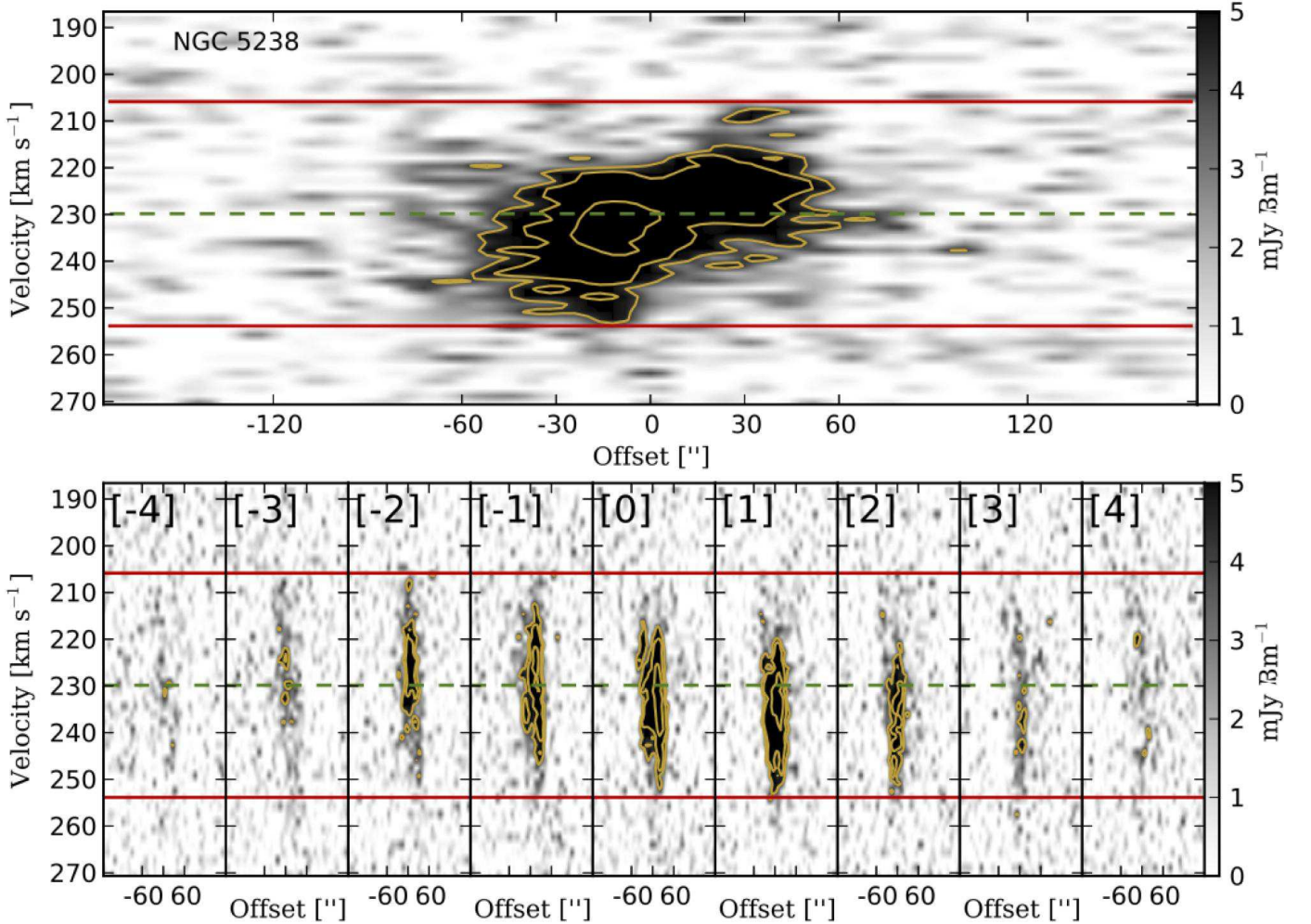


**Figure 8.** Spatially resolved P-V analysis of NGC 5238; all slices are the width of the H I synthesized beam ( $18''$ ). The top panel shows the major axis slice along a position angle  $20^\circ$  east of north. The bottom nine panels show the minor axis slices, each separated from one another by  $18''$ ; slice 0 passes through the middle of the major axis slice and through the H I mass surface density maximum. In all panels, the green line identifies the systemic velocity of the source; the red lines identify the maximal velocity extent to which rotation is evident; the yellow contours show (3, 5, 10) times the per-channel noise in the cube ( $1.4 \text{ mJy Bm}^{-1}$ ). From this analysis we infer a projected rotation velocity of  $24 \text{ km s}^{-1}$ , at a maximum angular extent of  $60''$ .

Each minor axis slice has a width equal to the H I beam size. In total, nine such minor axis slices are extracted; the central minor axis slice passes through the center of the major axis slice. These minor axis slices show the intensity-weighted H I velocity and dispersion at a given position in the disk. As demonstrated in Cannon et al. (2011a), Bernstein-Cooper et al. (2014), and McNichols et al. (2016), if projected rotation is present in a system, then the minor-axis slices will identify any such gradient as a change in the velocity of the H I centroid as a function of position of the slice.

In Figure 8 we present the results of this spatially resolved P-V analysis. The major axis P-V slice identifies a total velocity gradient of  $48 \text{ km s}^{-1}$ , spanning  $60''$  (1.3 kpc at the adopted distance of 4.51 Mpc). This is confirmed in the minor axis slices, which show a similar total velocity gradient across the disk. Note that the asymmetries of the NGC 5238 neutral gas disk result in some turnover in the centroid velocities of the H I gas in the most distant minor axis slices (numbers +4 and -4 in Figure 8); these slices are  $72''$  (1.57 kpc) from the slice center. From this analysis we conclude that NGC 5238

has a projected rotational velocity of  $24 \text{ km s}^{-1}$ , and that this rotation can be unambiguously identified to a maximum physical radius of 1.3 kpc.

As discussed at length in McNichols et al. (2016), the correction of the observed velocities for inclination is the most significant uncertainty in the analysis of the dynamics of low-mass galaxies. Following that work, we use the optical inclination derived in § 3.3 to correct the observed H I for projection effects and thus to determine the true rotational velocity. Our inclination value of  $(50 \pm 5)^\circ$  compares favorably with the value of  $55^\circ$  implied by the axial ratios derived from the UV images in Lee et al. (2011); our measurement agrees within  $\sim 5^\circ$  with the implied inclination of  $40^\circ$  from the Dale et al. (2009) IR apertures.

The resulting circular velocity of NGC 5238 is  $31 \pm 5 \text{ km s}^{-1}$ , measured to a maximum physical radius of 1.3 kpc using gas detected at  $3\sigma$  significance or higher. The implied dynamical mass using  $M = \frac{v^2 R}{G}$  is  $(3 \pm 1) \times 10^8 M_\odot$ . This can be compared to  $3.7 \times 10^8 M_\odot$  when also explicitly accounting for random motions in the H I gas as demonstrated in (Hoffman et al. 1996); for

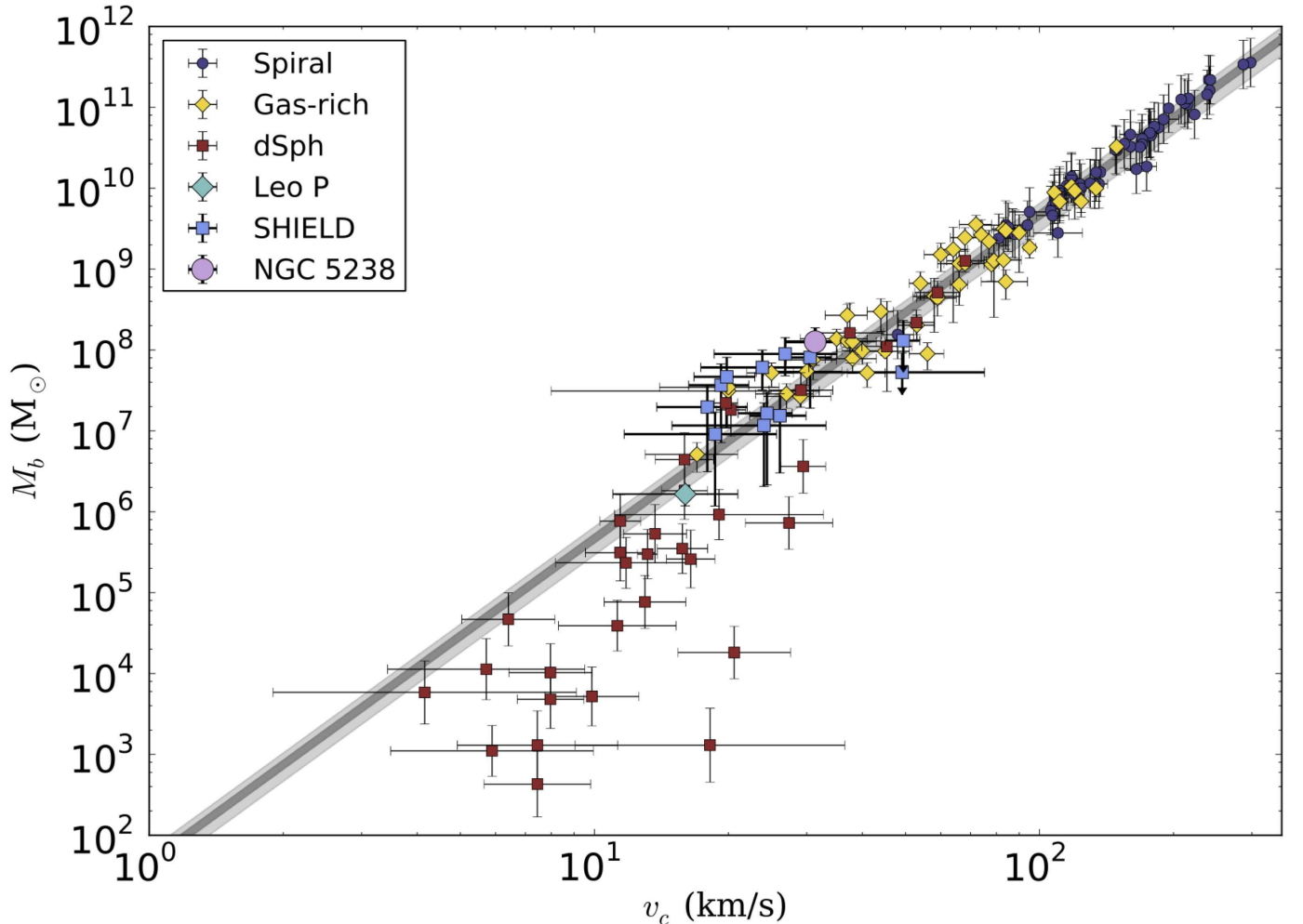


**Figure 9.** The Baryonic Tully-Fisher relation (BTFR) as derived in McNichols et al. (2016). The small points are drawn from McGaugh (2012); the purple circles correspond to spiral galaxies; the gold diamonds represent less massive gas-rich galaxies; the red squares represent spheroidal dwarf galaxies with no detectable H I. The cyan diamond represents Leo P, the slowest rotating and lowest-mass galaxy known to still be relatively rich with interstellar gas (Bernstein-Cooper et al. 2014). The blue squares represent the SHIELD galaxies. The large magenta circle is our new measurement for NGC 5238. The light and dark shaded gray regions represent the  $1\sigma$  and the  $3\sigma$  deviations from a fit of the BTFR to the gas-rich galaxy sample, respectively. Within measurement errors, NGC 5238 lies on this calibration of the BTFR.

this calculation we assume the average H I velocity dispersion throughout the disk ( $8.5 \text{ km s}^{-1}$ ; see Figure 4). Correcting the total H I mass for Helium and other metals (a 35% correction), the total gas mass of NGC 5238 is  $(3.7 \pm 0.3) \times 10^7 M_\odot$ . Using the stellar mass in Table 1, the total baryonic mass is  $1.3 \times 10^8 M_\odot$ ; NGC 5238 is dark-matter dominated at a roughly 2.4:1 ratio, a value like those found for the SHIELD galaxies in McNichols et al. (2016). These values allow us to place NGC 5238 on the baryonic Tully-Fisher relation (BTFR). As shown in Figure 9, NGC 5238 agrees with the calibration of the BTFR presented in McGaugh (2012) and updated to include the SHIELD sample in McNichols et al. (2016). NGC 5238 follows the same scaling relation between rotational velocity and baryonic mass as the SHIELD galaxies.

##### 5. CONTEXTUALIZING NGC 5238

NGC 5238 shares many physical characteristics with the most massive galaxies from the SHIELD sample. Formally, if the Right Ascension and Declination of

NGC 5238 placed it inside the ALFALFA survey footprint (Giovanelli et al. 2005), it would not have been not met all of the SHIELD survey selection criteria. It would meet the  $W_{50} < 65 \text{ km s}^{-1}$  line width criterion but would fail the H I mass criterion ( $\log[M_{\text{H I}}] < 10^{7.2}$ ); NGC 5238 is  $\sim 75\%$  too H I-massive to have been selected for SHIELD. Note, however, that stellar-based distances to many of the SHIELD galaxies (McQuinn et al. 2014) moved them further than the initial distance estimates upon selection. The final SHIELD sample presented in Teich et al. (2016) and McNichols et al. (2016) contains 4 sources with  $\log(M_{\text{H I}}) > 10^{7.2}$ ; one of these sources (AGC 749237) is more H I-massive than NGC 5238.

Qualitatively, the physical properties of NGC 5238 bridge the regime between the extremely low-mass SHIELD galaxies and the more massive dwarf irregular galaxies in the Local Group and beyond. As Figure 9 demonstrates, this source populates the region of the BTFR that is sparsely populated by the highest-mass SHIELD galaxies and the lowest-mass galaxies studied in McGaugh (2012). The H I disk of NGC 5238 is larger

(physical diameter  $\simeq 4$  kpc at largest extent) than those of all of the SHIELD galaxies except for AGC 749237, which is of comparable size. The peak H I column density in NGC 5238 is the same as the highest peaks seen in the SHIELD galaxies (AGC 110482 and AGC 749237). Interestingly, the kinematics of NGC 5238 are significantly more confused than those of the most massive SHIELD galaxies; AGC 749237, AGC 112521, and AGC 110482 show comparatively ordered rotation in two-dimensional velocity fields. NGC 5238, in contrast, shows complex kinematics; two- and three-dimensional rotationally-supported disk modeling fails in this comparatively massive source.

As discussed in Section 3.2, the FUV and H $\alpha$  star formation rates of NGC 5238 are higher than those of any of the SHIELD galaxies (Teich et al. 2016). The origin of the high star formation rate in NGC 5238 compared to those in the SHIELD galaxies is not immediately clear. There are no known galaxies cataloged in the NASA Extragalactic Database<sup>8</sup> within a projected separation of 300 kpc whose recessional velocities are within 100 km s<sup>-1</sup> of the  $V_{\text{HI}} = 232 \pm 1$  km s<sup>-1</sup> derived in this work (see discussions in Lelli et al. 2014 and Martinkus et al. 2015). While the outer H I disk of NGC 5238 does show some asymmetries, we do not detect unambiguous evidence for an ongoing tidal interaction at the current sensitivity and angular resolution of our VLA observations. We note that recent work suggests that interactions at large distances may not be important for star formation rates in dwarf galaxies (see, e.g., Pearson et al. 2016).

The distributed recent star formation in NGC 5238 differentiates it from most of the SHIELD galaxies. In those systems, almost all of the galaxies show H $\alpha$  emission that is concentrated to a few isolated HII regions or at most some faint diffuse emission. In contrast, NGC 5238 harbors widespread H $\alpha$  emission with both clustered and diffuse morphology. From the far-UV perspective, the SHIELD galaxies show a variety of morphologies; some sources have widespread far-UV emission throughout most of the inner disk, while others show only very faint far-UV emission. Again NGC 5238 stands out in a comparative sense: the entire inner disk is UV-bright, which is unlike the SHIELD galaxies.

## 6. CONCLUSIONS

We have presented new VLA H I spectral line observations of the nearby star-forming dwarf irregular galaxy NGC 5238. The data resolve the structure and dynamics of the neutral gas on spatial ( $\sim 400$  pc) and spectral (1.56 km s<sup>-1</sup> ch<sup>-1</sup>) scales that can be meaningfully compared to other major H I survey results. The outer portions of the neutral gas disk show significant asymmetries. The high mass surface density H I gas displays an interesting crescent-shaped morphology, with the highest H I column densities in excess of  $1.5 \times 10^{21}$  cm<sup>-2</sup>.

The new H I images are compared with images from HST, GALEX, and the Bok 2.3m telescope in order to study the nature of the recent star formation in NGC 5238. The stellar disk is resolved into multiple stellar clusters by the HST LEGUS images (Calzetti et al. 2015), and there is an exquisite match between the UV-bright stellar population and the H $\alpha$  emission that per-

meates much of the inner disk. The most luminous UV clusters are associated with high column density gas ( $N_{\text{HI}} \simeq 10^{21}$  cm<sup>-2</sup>), but there are a significant number of UV-bright stars in regions of lower column densities as well. The regions of highest H I mass surface densities are not co-spatial with the most luminous UV and H $\alpha$  sources.

We quantify the degree of co-spatiality between H I and star formation tracers using both radially averaged and pixel-by-pixel star formation rate density analyses. The far-UV results are qualitatively similar to those found for the properties of star formation in the SHIELD galaxies by Teich et al. (2016). The H $\alpha$  emission in NGC 5238 is significantly more widespread than in the SHIELD galaxies. The Kennicutt-Schmidt indices are  $N = 1.46 \pm 0.02$  and  $N = 1.17 \pm 0.01$  in the FUV and in H $\alpha$ , respectively. The H $\alpha$ -based value is steeper than the value found for the composite SHIELD sample ( $N = 0.68 \pm 0.04$ ) in Teich et al. (2016), but is in good agreement with the values found in the individual SHIELD galaxies with the highest star formation rates and the highest H I mass surface densities.

The complex neutral gas dynamics of NGC 5238 preclude an unambiguous two or three-dimensional model of the rotation of the source; degeneracies persist between inclination and rotation velocity. As for the SHIELD galaxies analyzed in McNichols et al. (2016), we use spatially-resolved position velocity analysis to estimate the projected rotation velocity of the galaxy. We correct this value for inclination based on an elliptical fit to the red stellar population seen by HST. The resulting rotational velocity  $V_{\text{rot}} = (31 \pm 5)$  km s<sup>-1</sup> implies a total dynamical mass of  $3 \times 10^8 M_{\odot}$ . Comparing to the sum of the neutral gas and stellar masses, NGC 5238 is dark matter dominated at a ratio of roughly 2.4:1. The galaxy falls on the baryonic Tully-Fisher relation as presented in McNichols et al. (2016).

NGC 5238 is an intriguing system that warrants further study. Higher angular resolution H I imaging could reveal small-scale feedback processes between the multiple stellar clusters and the surrounding neutral gas. The stellar population is well-resolved by HST, making possible a detailed study of the recent star formation history. The significant nebular emission would facilitate detailed and resolved analysis of the chemical composition of the system. The preliminary estimates of the metallicity ( $Z \simeq 19\% Z_{\odot}$ ; Moustakas & Kennicutt 2006) place this system near the empirical boundary below which CO emission becomes extremely difficult to detect in dwarf galaxies (e.g., Taylor et al. 1998; Leroy et al. 2005; Schruba et al. 2012). While single-dish CO observations by Leroy et al. (2005) failed to detect NGC 5238, the high star formation rate and significant H I mass surface densities suggest that targeted interferometric observations could be fruitful.

The authors are immensely grateful to the National Radio Astronomy Observatory for making the ‘‘Observing for University Classes’’ program available to the astronomical and teaching communities. We would like to personally thank Vivek Dhawan, Miller Goss, Christopher Hales, Amy Kimball, Chris Langley, Emmanuel Momjian, Jürgen Ott, Lorant Sjouwerman, and Gustaaf van Moorsel for making our visit to the Domenici Science

<sup>8</sup> <http://ned.ipac.caltech.edu>

Operations Center and the VLA site productive and enjoyable. We are grateful to Macalester College for supporting this project. We would like to thank the referee for a prompt and insightful report that helped to improve this manuscript.

Funding for the Sloan Digital Sky Survey IV has been provided by the Alfred P. Sloan Foundation, the U.S. Department of Energy Office of Science, and the Participating Institutions. SDSS-IV acknowledges support and resources from the Center for High-Performance Computing at the University of Utah. The SDSS web site is [www.sdss.org](http://www.sdss.org).

SDSS-IV is managed by the Astrophysical Research Consortium for the Participating Institutions of the SDSS Collaboration including the Brazilian Participation Group, the Carnegie Institution for Science, Carnegie Mellon University, the Chilean Participation Group, the French Participation Group, Harvard-Smithsonian Center for Astrophysics, Instituto de Astrofísica de Canarias, The Johns Hopkins University, Kavli Institute for the Physics and Mathematics of the Universe (IPMU) / University of Tokyo, Lawrence Berkeley National Laboratory, Leibniz Institut für Astrophysik Potsdam (AIP), Max-Planck-Institut für Astronomie (MPIA Heidelberg), Max-Planck-Institut für Astrophysik (MPA Garching), Max-Planck-Institut für Extraterrestrische Physik (MPE), National Astronomical Observatory of China, New Mexico State University, New York University, University of Notre Dame, Observatório Nacional / MCTI, The Ohio State University, Pennsylvania State University, Shanghai Astronomical Observatory, United Kingdom Participation Group, Universidad Nacional Autónoma de México, University of Arizona, University of Colorado Boulder, University of Oxford, University of Portsmouth, University of Utah, University of Virginia, University of Washington, University of Wisconsin, Vanderbilt University, and Yale University.

Facilities: VLA, HST, GALEX, Bok 2.3m

#### REFERENCES

- Asplund, M., Grevesse, N., Sauval, A. J., & Scott, P. 2009, *ARA&A*, 47, 481
- Begum, A., Chengalur, J. N., Karachentsev, I. D., Sharina, M. E., & Kaisin, S. S. 2008, *MNRAS*, 386, 1667
- Bernstein-Cooper, E. Z., Cannon, J. M., Elson, E. C., et al. 2014, *AJ*, 148, 35
- Bigiel, F., Leroy, A., Walter, F., et al. 2008, *AJ*, 136, 2846
- Calzetti, D., Lee, J. C., Sabbi, E., et al. 2015, *AJ*, 149, 51
- Cannon, J. M., Most, H. P., Skillman, E. D., et al. 2011, *ApJ*, 735, 35
- Cannon, J. M., Giovanelli, R., Haynes, M. P., et al. 2011, *ApJ*, 739, L22
- Cannon, J. M., Martinkus, C. P., Leisman, L., et al. 2015, *AJ*, 149, 72
- Cook, D. O., Dale, D. A., Johnson, B. D., et al. 2014, *MNRAS*, 445, 881
- Cook, D. O., Dale, D. A., Johnson, B. D., et al. 2014, *MNRAS*, 445, 899
- Dalcanton, J. J., Williams, B. F., Seth, A. C., et al. 2009, *ApJS*, 183, 67
- Dale, D. A., Cohen, S. A., Johnson, L. C., et al. 2009, *ApJ*, 703, 517
- Dreyer, J. L. E. 1888, *MmRAS*, 49, 1
- Elmegreen, B. G., & Hunter, D. A. 2015, *ApJ*, 805, 145
- Giovanelli, R., Haynes, M. P., Kent, B. R., et al. 2005, *AJ*, 130, 2598
- Hagen, C., Cannon, J. M., Cave, I., et al. 2014, *American Astronomical Society Meeting Abstracts #223, 223, #355.16*
- Hao, C.-N., Kennicutt, R. C., Johnson, B. D., et al. 2011, *ApJ*, 741, 124
- Haurberg, N. C. 2013, Ph.D. Thesis, Indiana University
- Hoffman, G. L., Salpeter, E. E., Farhat, B., et al. 1996, *ApJS*, 105, 269
- Hunter, D. A., Elmegreen, B. G., & Baker, A. L. 1998, *ApJ*, 493, 595
- Hunter, D. A., Ficut-Vicas, D., Ashley, T., et al. 2012, *AJ*, 144, 134
- Ianjamasimanana, R., de Blok, W. J. G., Walter, F., et al. 2015, *AJ*, 150, 47
- Jorsater, S., & van Moorsel, G. A. 1995, *AJ*, 110, 2037
- Kennicutt, R. C., Jr., Armus, L., Bendo, G., et al. 2003, *PASP*, 115, 928
- Kennicutt, R. C., Jr., Lee, J. C., Funes, J. G., et al. 2008, *ApJS*, 178, 247-279
- Kennicutt, R. C., Jr. 1998, *ARA&A*, 36, 189
- Kennicutt, R. C., Calzetti, D., Aniano, G., et al. 2011, *PASP*, 123, 1347
- Kirby, E. M., Koribalski, B., Jerjen, H., & López-Sánchez, Á. 2012, *MNRAS*, 420, 2924
- Lee, J. C., Gil de Paz, A., Kennicutt, R. C., Jr., et al. 2011, *ApJS*, 192, 6
- Lelli, F., Verheijen, M., & Fraternali, F. 2014, *MNRAS*, 445, 1694
- Leroy, A., Bolatto, A. D., Simon, J. D., & Blitz, L. 2005, *ApJ*, 625, 763
- Marble, A. R., Engelbracht, C. W., van Zee, L., et al. 2010, *ApJ*, 715, 506
- Martinkus, C., Cannon, J. M., McQuinn, K. B., et al. 2015, *American Astronomical Society Meeting Abstracts*, 225, 248.21
- McGaugh, S. S. 2012, *AJ*, 143, 40
- McNichols, A. T., Teich, Y. G., Nims, E., Cannon, J. M., et al. 2016, *ApJ*, in press (ArXiv/1609.05376)
- McQuinn, K. B. W., Cannon, J. M., Dolphin, A. E., et al. 2014, *ApJ*, 785, 3
- McQuinn, K. B. W., Skillman, E. D., Dolphin, A. E., & Mitchell, N. P. 2015, *ApJ*, 808, 109
- Mogotsi, K. M., de Blok, W. J. G., Caldú-Primo, A., et al. 2016, *AJ*, 151, 15
- Moustakas, J., & Kennicutt, R. C., Jr. 2006, *ApJS*, 164, 81
- Ott, J., Stilp, A. M., Warren, S. R., et al. 2012, *AJ*, 144, 123
- Pearson, S., Besla, G., Putman, M. E., et al. 2016, *MNRAS*, 459, 1827
- Roychowdhury, S., Chengalur, J. N., Kaisin, S. S., & Karachentsev, I. D. 2014, *MNRAS*, 445, 1392
- Schmidt, M. 1959, *ApJ*, 129, 243
- Schruba, A., Leroy, A. K., Walter, F., et al. 2012, *AJ*, 143, 138
- Skillman, E. D. 1987, *NASA Conference Publication*, 2466, 263
- Swaters, R. A., van Albada, T. S., van der Hulst, J. M., & Sancisi, R. 2002, *A&A*, 390, 829
- Tamburro, D., Rix, H.-W., Leroy, A. K., et al. 2009, *AJ*, 137, 4424
- Taylor, C. L., Kobulnicky, H. A., & Skillman, E. D. 1998, *AJ*, 116, 2746
- Teich, Y. G., McNichols, A.T., Nims, E., Cannon, J. M., et al. 2016, *ApJ*, in press (ArXiv/1609.05375)
- Thuan, T. X., Lipovetsky, V. A., Martin, J.-M., & Pustilnik, S. A. 1999, *A&AS*, 139, 1
- Tully, R. B., & Fisher, J. R. 1977, *A&A*, 54, 661
- Tully, R. B., Rizzi, L., Shaya, E. J., et al. 2009, *AJ*, 138, 323
- van Zee, L., Haynes, M. P., Salzer, J. J., & Broeils, A. H. 1997, *AJ*, 113, 1618
- York, D. G., Adelman, J., Anderson, J. E., Jr., et al. 2000, *AJ*, 120, 1579